Development of phase-time-resolved X-ray ferromagnetic resonance techniques based on synchrotron radiation*

YUAN Yanan[1], WANG Siyu[1], QIN Chunyu[1], YAN Penghui[1], FU Siyuan[1], WANG Yamei[2], CAO Jiefeng[2], LI Qian[1, *]

1. National Synchrotron Radiation Laboratory, School of Nuclear Science and Technology, University of Science and Technology of China, Hefei, 230029, China
2. Shanghai Synchrotron Radiation Facility, Shanghai Advanced Research Institute, Chinese Academy of Sciences, Shanghai 201204, China

Abstract

Ultrafast magnetization dynamics represent the forefront of modern spintronics and magnetic materials research, addressing the response and evolution of magnetic moments in magnetic systems on a femtosecond-to-nanosecond timescale. To elucidate such ultrafast magnetic processes, a variety of time-resolved experimental techniques have been developed. Among these techniques, synchrotron-based X-ray ferromagnetic resonance (XFMR) combines microwave-driven ferromagnetic resonance (FMR) with X-ray magnetic circular dichroism (XMCD) detection, enabling element-, valence-, and lattice space-resolved measurements of magnetization precession on a picosecond timescale and providing direct access to both the amplitude and the phase of the dynamic magnetic moment. In this work, we developed a picosecond time-resolved XFMR platform at the BL07U vector magnet beamline of the Shanghai Synchrotron Radiation Facility (SSRF). The system employs a lock-in modulation detection scheme precisely synchronized with the storage-ring master clock, realizing stable excitation and detection of spin precession in magnetic materials up to 6 GHz, with the background noise effectively suppressed to 30 fA, and an overall phase time resolution better than 10 ps. The successful implementation of this technique establishes a state-of-the-art XFMR capability in China, achieving internationally competitive performance in both temporal resolution and detection sensitivity. This development provides a strong experimental foundation

---

* The paper is an English translated version of the original Chinese paper published in Acta Physica Sinica. Please cite the paper as: YUAN Yanan[1], WANG Siyu[1], QIN Chunyu[1], YAN Penghui[1], FU Siyuan[1], WANG Yamei[2], CAO Jiefeng[2], LI Qian[1, *], **Development of phase-time-resolved X-ray ferromagnetic resonance techniques based on synchrotron radiation**. *Acta Phys. Sin.*, 2026, 75(6):060805. doi: 10.7498/aps.75.20251577

for future research on spin current and orbital current detection, as well as ferrimagnetic and antiferromagnetic dynamics.

Keywords: ultrafast magnetization dynamics; synchrotron radiation; X-ray ferromagnetic resonance; phase-time resolution

DOI: 10.7498/aps.75.20251577

CSTR: 32037.14.aps.75.20251577

1 Introduction

Understanding the ultrafast evolution of magnetic moments in magnetic materials is a core focus of contemporary condensed matter physics and spintronics. The response of magnetic moments on femtosecond to nanosecond timescales governs angular momentum transfer, energy relaxation, and magnetic damping. These processes are fundamental to the design of next-generation high-speed, low-energy spintronic devices and magnetic storage technologies[1-3]. Over the past two decades, rapid advances in femtosecond laser optics, microwave electronics, and coherent X-ray science have transformed magnetic dynamics research. The field has progressed from quasi-static measurements to multidimensional time-resolved detection with element selectivity and phase resolution. This shift has significantly enhanced our understanding of ultrafast dynamic mechanisms in magnetic systems.

In traditional all-optical detection methods, time-resolved magneto-optical Kerr effect (TR-MOKE) offers sub-picosecond time resolution and flexible experimental geometry. It is widely used for dynamic observations of nanomagnetic structures[4,5]. However, visible light photons have low energy (approximately 1-2 eV). Consequently, they cannot probe core-level transitions or specific elemental magnetic moments within magnetic materials. The measured signals mostly reflect overall magnetization responses, making it difficult to distinguish the independent contributions of each element in multi-component systems. Another typical approach involves ferromagnetic resonance (FMR) based on microwave excitation[6], as well as spin pumping[7,8] and spin-torque ferromagnetic resonance (ST-FMR)[9]. These methods drive magnetic moments into Larmor precession under an external magnetic field using microwave magnetic fields or radio-frequency currents. They have become important tools for quantitatively characterizing anisotropy fields, damping coefficients, spin mixing conductance, and spin-orbit torques[10]. These techniques offer high testing efficiency, strong signal-to-noise ratios, and suitability for routine laboratory and in-situ device characterization. However, similar to TR-MOKE, they measure the macroscopic average magnetic response of the sample. In recent years, tabletop ultrafast magnetic detection technologies based on high-harmonic generation (HHG) extreme ultraviolet (EUV) sources have developed rapidly. High harmonics generated by femtosecond lasers can cover the absorption edges of 3d transition metals, enabling element-selective detection under laboratory conditions[11,12]. Nevertheless, such systems still face challenges in high-precision quantitative measurements due to low photon flux, limited energy stability, and insufficient signal-to-noise ratios.

To overcome these limitations and obtain deeper element- and layer-resolved magnetic dynamic information, researchers have turned to X-ray magnetic spectroscopy techniques. Synchrotron radiation X-ray ferromagnetic resonance (XFMR) combines microwave-excited FMR with element-selective X-ray magnetic circular dichroism (XMCD) detection. This technique can directly measure the precession amplitude and phase of specific elements on picosecond timescales. It offers both element selectivity and high sensitivity[2,13,14]. XFMR is particularly suitable for separating the dynamic contributions of each layer or element in multilayer films or alloy systems.

XFMR imposes high requirements on the time structure and stability of synchrotron radiation facilities. Thanks to the development of major international synchrotron sources, this technology has seen continuous progress in recent years. In 2004, Bailey et al.[15] achieved independent precession measurements of Ni and Fe elements in $Ni_{81}Fe_{19}$ alloys for the first time at the 4-ID-C beamline of the Advanced Photon Source (APS) at Argonne National Laboratory in the United States. Subsequently, Boero, Goulon, and colleagues performed similar XFMR measurements in 2005 at the ID08 beamline of the European Synchrotron Radiation Facility (ESRF)[16,17]. However, these pioneering works employed time-averaged measurement methods, thereby lacking information on the phase of magnetic moment precession. The work that achieved time-resolved and layer-resolved XFMR was conducted by Arena et al.[18] in 2006. They studied ferromagnetic resonance in ferromagnetic/non-magnetic/ferromagnetic trilayer systems at the National Synchrotron Light Source (NSLS) at Brookhaven National Laboratory in the United States. This study demonstrated for the first time that XFMR could simultaneously obtain magnetization and phase information. Later, the I10 beamline at the Diamond Light Source in the United Kingdom reported on spin pumping[13] and spin current transport in topological insulators[19], antiferromagnetic metals[20], and antiferromagnetic insulators[21]. They developed thickness-resolved magnetic dynamics measurement technology based on X-ray elastic resonant scattering ferromagnetic resonance[22]. The 4.0.2 beamline at the Advanced Light Source (ALS) in the United States achieved interlayer dynamic coupling[23] and spin current transport in paramagnetic and antiferromagnetic insulators[24,25]. The 2A-MS beamline at the

Pohang Light Source (PLS-II) in South Korea integrated XMCD/XFMR capabilities[26]. In recent years, China has also made significant progress in this field. Relying on the BL08U and BL07U beamlines at the Shanghai Synchrotron Radiation Facility (SSRF), research teams developed an XFMR apparatus with an FMR frequency of 2.5 GHz. They achieved Ni element-resolved magnetization precession measurements in $Ni_{81}Fe_{19}$[27]. This achievement filled a domestic gap and provided key support for element-resolved ultrafast magnetic dynamics research.

This paper focuses on the SSRF BL07U vector magnet experimental station[28,29]. We performed systematic optimization and functional redesign based on the successful construction of the previous XFMR apparatus. By introducing lock-in amplification modulation detection, we significantly improved the signal-to-noise ratio (SNR). We also optimized the coplanar waveguide structure to achieve highly stable microwave magnetic field distribution across a wide frequency band. This enhancement increased the excitation magnetic field strength and improved the sensitivity and resolution of X-ray detection. The operating frequency range of the system was extended to 6 GHz. It can stably excite and precisely detect spin precession of magnetic elements. Background noise was effectively suppressed to the order of 30 fA, and the overall phase time resolution accuracy was better than 10 ps. The comprehensive performance of this platform has reached and partially surpassed international advanced levels. It lays a solid experimental foundation for subsequent magnetic dynamics research involving small signal resolution.

2 Principles of XFMR Technology and Experimental Methods

2.1 Basic Principles of XFMR

X-ray ferromagnetic resonance is an element-resolved dynamic magnetic detection technique that combines ferromagnetic resonance with X-ray magnetic circular dichroism[14,30]. As shown in Figure 1, this method drives magnetic moments into ferromagnetic resonance precession using a microwave field. It utilizes the high brightness and circular polarization characteristics of synchrotron radiation X-rays to achieve time- and phase-resolved measurements of magnetization precession at specific element absorption edges. The physical essence of ferromagnetic resonance is the precession behavior of magnetic moments under the combined action of an external magnetic field H_0 and a microwave field H_{rf}. When the microwave frequency matches the intrinsic precession frequency of the sample spin system, the system absorbs energy and enters a resonance state. Its dynamics can be described by the

Landau-Lifshitz-Gilbert (LLG) equation[31]:

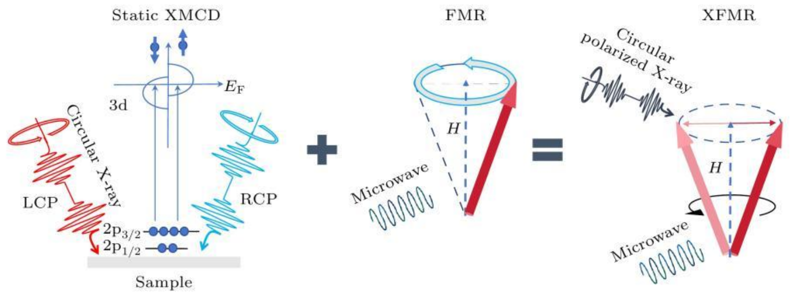

Fig. 1 Schematic diagram of the XFMR measurement principle.

$$\frac{\mathrm{d}\boldsymbol{M}}{\mathrm{d}t} = -\gamma \boldsymbol{M} \times \boldsymbol{H}_{\text{eff}} + \frac{\alpha}{\boldsymbol{M}_{\text{s}}} \boldsymbol{M} \times \frac{\mathrm{d}\boldsymbol{M}}{\mathrm{d}t}, \quad (1)$$

Here, γ denotes the gyromagnetic ratio, α represents the damping coefficient, $\boldsymbol{H}_{\text{eff}}$ is the total effective magnetic field acting on the magnetization M, and M_s is the saturation magnetization. The perturbation component $\boldsymbol{m}(t)$ of the magnetization vector $\boldsymbol{M}(t) = \boldsymbol{M}_{\text{s}}\hat{z} + \boldsymbol{m}(t)$ undergoes periodic precession over time under resonance conditions. Its amplitude and phase reflect the internal magnetic anisotropy, damping mechanisms, and coupling characteristics of the material. In this state, $\omega = \gamma\sqrt{(H_0 + H_{\text{k}})(H_0 + H_{\text{k}} + 4\pi M_{\text{eff}})}$, where H_0 is the external magnetic field, H_{k} is the effective anisotropy field, and $4\pi M_{\text{eff}}$ is the effective demagnetizing term.

The XMCD effect arises from differences in circularly polarized light absorption under spin-orbit coupling. By altering the light helicity (σ^+/σ^-) or the sample magnetization direction (M/-M), one can obtain element-specific magnetic absorption differences. These differences reflect the magnitude and direction of the sample magnetic moment, as well as spin-orbit contributions. When circularly polarized X-rays incident on magnetic materials, their absorption coefficients vary with the magnetic moment direction:

$$\Delta\mu(E) = \mu^+(E) - \mu^-(E) \propto \boldsymbol{M} \cdot \hat{\boldsymbol{k}}, \quad (2)$$

Here, $\mu^+(E)$ and $\mu^-(E)$ denote the absorption coefficients for left- and right-handed circularly polarized light, respectively; $\hat{\boldsymbol{k}}$ represents the direction of light propagation. When the probe energy is tuned to the absorption edge of a specific element (such as the L_3 edge of Fe, Co, or Ni), independent detection of the magnetic moment projections for different elements becomes feasible. Under the small-angle precession approximation, the XMCD signal intensity exhibits sinusoidal periodic modulation over time:

$$I(t) = A\sin(\omega t + \varphi), \quad (3)$$

Here, A denotes the precession amplitude, and φ represents the phase delay. By analyzing the amplitude-phase relationship, one can directly extract coupling effects between different elements or layers. Consequently, by combining FMR with XMCD, XFMR technology not only detects the resonance of total magnetization but also distinguishes magnetic moment responses of different atomic species, valence states, or lattice sites through the element selectivity of XMCD. This capability enables element-resolved, layer-resolved, and sublattice-resolved dynamic spectroscopic characterization, establishing XFMR as a crucial experimental tool for investigating spin dynamics within ferromagnetic, ferrimagnetic, and certain antiferromagnetic systems.

2.2 Principles of Pump-Probe Technology

The time-resolution capability of XFMR relies on precise control of the phase relationship between microwave excitation (pump) and synchrotron X-ray detection (probe). By adjusting the phase delay between these two components, researchers can measure the entire process of magnetic moment precession. Specifically, as illustrated in Figure 2, this method leverages the strict temporal structure of the storage ring (RF master clock) and the phase synchronization capability of the phase modulation system. A phase shifter introduces a controllable phase shift (or equivalent time delay), ensuring that the microwaves input into the sample have a specific phase shift relative to the X-ray pulses. Each phase shift corresponds to a specific phase point sampled within the precession cycle. By acquiring XMCD signals at multiple phase settings, the X-ray pulses can probe the progressive deviations of the sample throughout the precession cycle. Connecting these measurement points from different phases in chronological order allows for the reconstruction of the complete curve describing magnetic moment precession over time. In 2006, Arena et al.[18] recorded sinusoidal oscillations in the XMCD signals of Ni, Fe, and Co by varying the relative delay between microwaves and X-rays. This successfully covered the entire precession cycle, demonstrating the experimental feasibility of time-resolved XFMR technology. This method imposes stringent requirements on the temporal structure and operating modes of synchrotron radiation sources to ensure the temporal stability of light pulses.

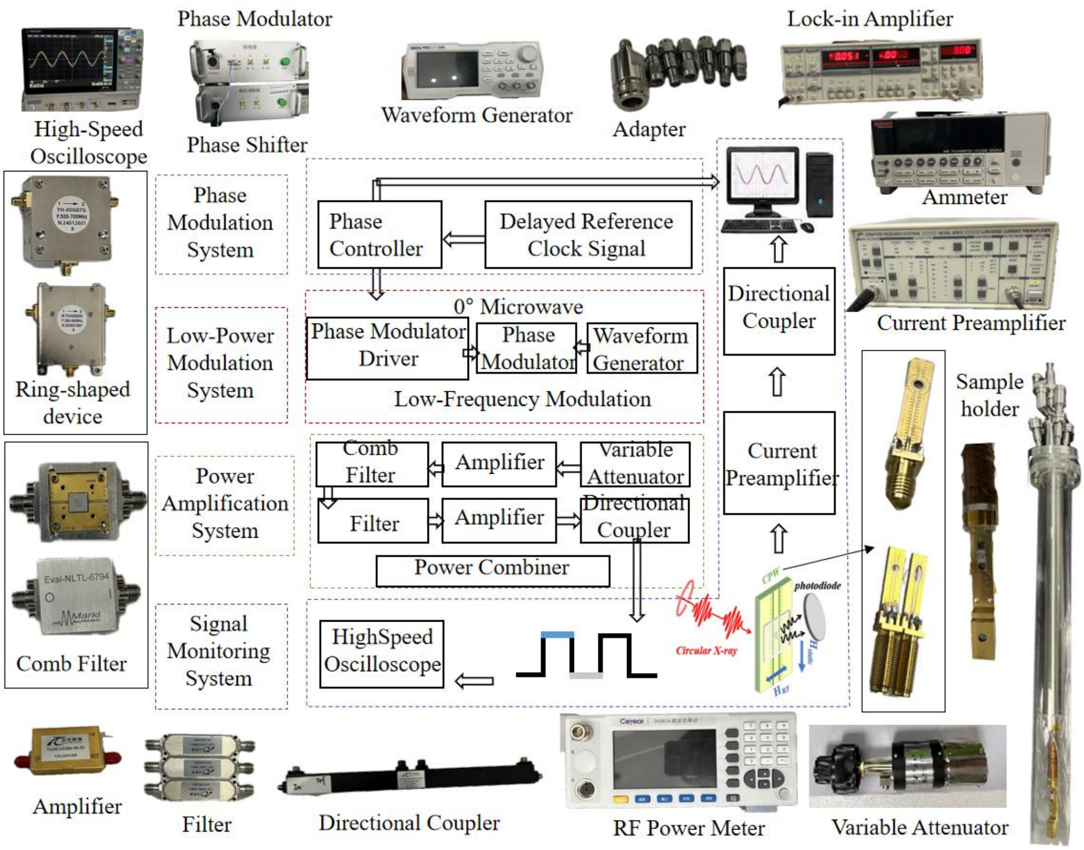

Fig. 2 System configuration breakdown and corresponding equipment display.

2.3 Lock-in Amplification Modulation Detection

XFMR signals typically constitute only about 1% of static XMCD signals, presenting significant challenges for signal-to-noise ratio. To address this, this study employs a lock-in amplifier for microwave modulation detection to significantly enhance signal extraction. The specific implementation involves applying low-frequency phase modulation at 10-1000 Hz to the input phase-delayed microwave signal using a waveform generator. This causes the microwave output from the phase modulator in the small-signal modulation system to alternate with 180° phase reversal. The lock-in amplifier (LIA) uses this modulation frequency as a reference to coherently extract the signal from the photodiode (PD) output, effectively suppressing background noise. Since the XMCD signal is proportional to the projection of the magnetic moment along the light incidence direction, the LIA output signal $I_{\text{XFMR}} = I^{+} - I^{-}$ can detect the difference in X-ray absorption on both sides of the precession cone when the magnetic moment precesses. By gradually delaying the phase of the radiofrequency field relative to the X-ray pulses, the complete precession cycle can be recorded.

2.4 Dynamic Signal Detection Methods

Dynamic XFMR signals can be detected using two geometric configurations, as shown in Figure 3: one measures the fluorescence yield (FY) generated by photons directly exciting the absorbing material, and the other measures the luminescence yield (LY) from the substrate beneath the thin film in a transmission geometry. In the LY mode, the sample is mounted on a coplanar waveguide (CPW). A tapered hole in the center conductor allows X-rays to penetrate the waveguide and irradiate the sample, while a photodiode mounted behind the hole collects the signal. The FY mode is similar to the LY mode, except the photodiode is positioned at an angle in front of the sample to detect the FY signal from the thin film. In both geometric configurations, XFMR measurements are performed with fixed helicity of the incident light, with the magnetic orientation of the thin film aligned along the CPW axis (*z*-axis). When radiofrequency current is applied to the CPW axis, it generates a radiofrequency magnetic field (RF magnetic field, denoted as H_{rf}) within the sample layer, thereby inducing resonant excitation of the magnetization direction. When the incident beam is perpendicular to the CPW axis, the magnetization component orthogonal to the static magnetic field and aligned with the X-ray direction during RF-induced precession can be detected. This switchable design ensures that XFMR testing is compatible with various sample thicknesses and absorption coefficients, guaranteeing high signal intensity while enhancing the geometric flexibility of the test setup.

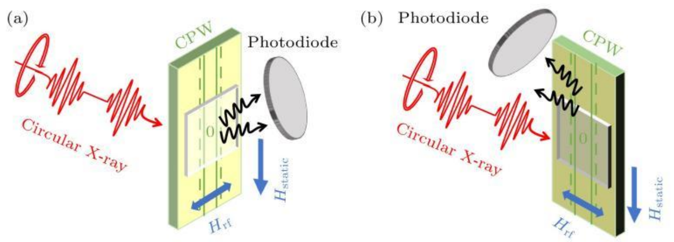

Fig. 3 Schematic diagram of the XFMR measurement mode: (a) The luminescence fluorescence method (LY); (b) the fluorescence method (FY).

2.5 Waveguide Design and Optimization

To achieve a waveguide structure integrating GHz microwave excitation with X-ray detection, we designed and fabricated a perforated grounded coplanar waveguide (GCPW) suitable for XFMR measurements. This waveguide employs a planar resonant structure capable of transmitting high-frequency signals. Through-holes are drilled at specific positions along the central signal line, allowing X-rays to pass through these apertures and irradiate the surface of the magnetic sample, where signals are collected by a photodiode. Figure 4 illustrates the simulated microwave magnetic field distribution in the cross-section of the perforated GCPW substrate at various frequencies. Simulation results indicate the presence of a microwave magnetic field stagnation point at the ground terminal of the coplanar waveguide signal conductor. A consistent microwave magnetic field intensity is maintained at this location across different microwave frequencies, whereas the field distribution far from the junction is significantly influenced by frequency. The non-metallic through-holes are positioned near the stagnation point, effectively ensuring broadband stability of the microwave magnetic field at the hole centers. By continuously adjusting the shape of the non-metallic through-holes, we found that using tapered holes reduces the aperture size at the signal conductor. This design effectively reduces microwave loss and significantly enhances microwave magnetic field intensity, thereby addressing the challenge of performing GHz spin precession measurements at higher frequencies with existing perforated waveguides. This perforated GCPW structure, tailored for synchrotron radiation X-ray measurements, not only exhibits excellent microwave magnetic field stability over a broad bandwidth but also significantly amplifies the field intensity. Consequently, it improves the sensitivity and resolution of synchrotron X-ray measurements, providing a new hardware platform for the application of this technology.

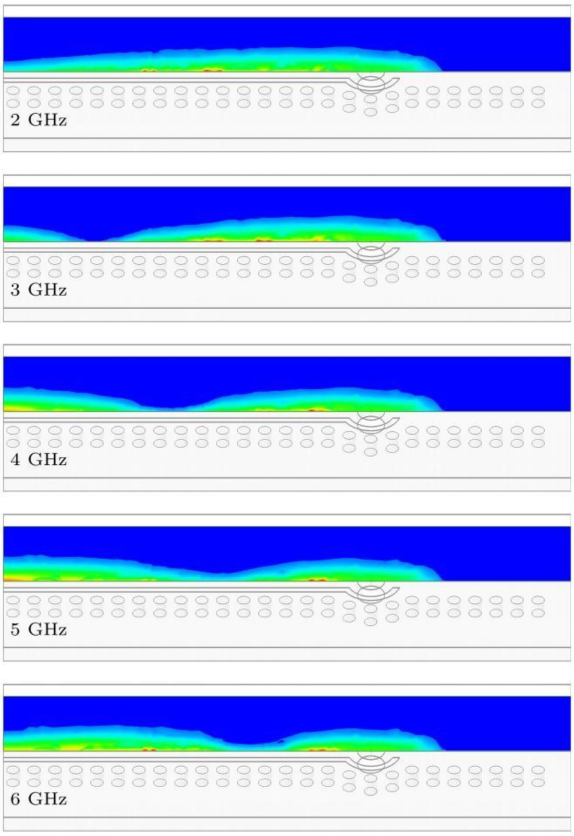

Fig. 4 Simulated microwave magnetic field distribution across the substrate cross-section of the perforated grounded coplanar waveguide at various frequencies.

2.6 Composition of the Experimental System and Synchronization Scheme

Integrating the pump-probe technique, lock-in amplification modulation detection, and novel waveguide design, we independently constructed an XFMR system with time and phase resolution at the BL07U beamline of the Shanghai Synchrotron Radiation Facility (Figure 5). Figure 6 illustrates the overall system architecture, which primarily comprises a phase modulation system, a small-signal modulation system, a power amplification system, and a signal monitoring system. The system extracts a microwave clock signal from the synchrotron accelerator, synchronized with the pulsed X-rays. This microwave clock signal undergoes phase delay, power gain, and frequency multiplication to generate microwave signals with adjustable frequency and phase. Specifically, an integrated high-frequency microwave amplifier, combining power amplification, comb generation, and filtering functions, increases the power (up to 3000 mW) and adjusts the frequency (to 1, 2, 3, 4, 5, or 6 GHz). This ensures the generated microwave matches the ferromagnetic resonance frequency of the sample, inducing sufficient precession angles in the sample magnetic moment. We input this microwave into a perforated planar resonant waveguide to excite GHz spin precession in the magnetic sample under test. Simultaneously, circularly polarized X-ray pulses incident on the perforation of the planar resonant waveguide detect the transient signals of spin precession in the ferromagnetic layer. This system achieves design goals for time synchronization, phase control, and high signal-to-noise ratio detection. It offers high reproducibility and sensitivity, providing a crucial experimental tool for investigating magnetic dynamics.

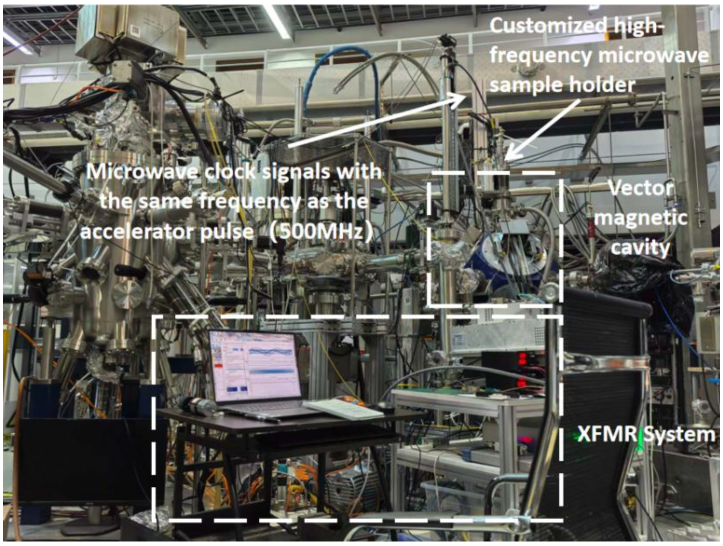

Fig. 5 Experimental setup at BL07U of the SSRF.

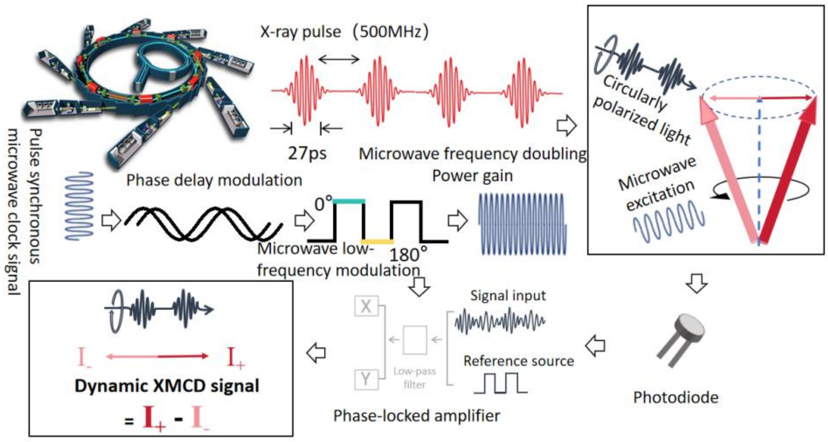

Fig. 6 Overall architecture diagram of the XFMR measurement system.

3 Experimental System and Measurement Results

To validate the system performance, we conducted XFMR measurements using a typical ferrimagnetic insulator, $Y_3Fe_5O_{12}$ (YIG), thin film as the sample. Figure 7 presents the phase delay scans measured at the Fe L_3 edge (photon energy ≈ 707.8 eV) under the resonant magnetic fields corresponding to ferromagnetic resonance at 0.5, 2, 4, and 6 GHz. As described by magnetization dynamics theory, the electron spin magnetic moments continuously precess around the effective field under the combined influence of the microwave magnetic field and the static magnetic field. Consequently, the component of the magnetic moment along the X-ray direction oscillates periodically. We fitted the experimental data with sinusoidal curves to facilitate observation. The phase delay scans exhibit distinct periodic behavior with a period of 2000 ps and its $1/N$ submultiples (N = frequency f / 0.5 GHz) corresponding to the respective excitation frequencies. This sinusoidal waveform reflects the oscillatory nature of the precessional motion.

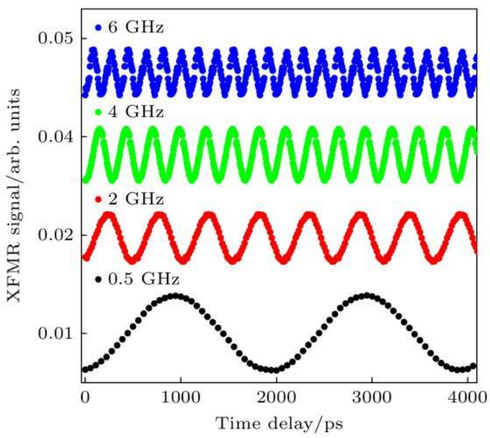

Fig. 7 Phase delay scan of the system at the corresponding resonance fields at 0.5, 2, 4, and 6 GHz at the Fe L_3 edge.

Subsequently, phase delay scans were performed at the Fe L_3 edge under varying resonant magnetic field conditions (Fig. 8(a)). Each scan was completed within a fixed bias magnetic field range of 11.2—19.6 Oe (1 Oe = $10^3/(4\pi)$ A/m). The phase delay curves exhibited distinct oscillations with a period of approximately 2000 ps, corresponding to the 0.5 GHz excitation frequency of the applied microwave. By fitting each curve with a sinusoidal function, the precession amplitude (Fig. 8(b)) and phase (Fig. 8(c)) for each magnetic field were extracted. The results indicate that the absorption amplitude follows a typical Lorentzian line shape as the magnetic field varies, whereas the phase displays an S-shaped magnetic field dependence. This includes a phase jump of approximately 180 ° near the resonance point, which can be accurately described by an arctangent function. Such characteristics are typical of damped harmonic motion.

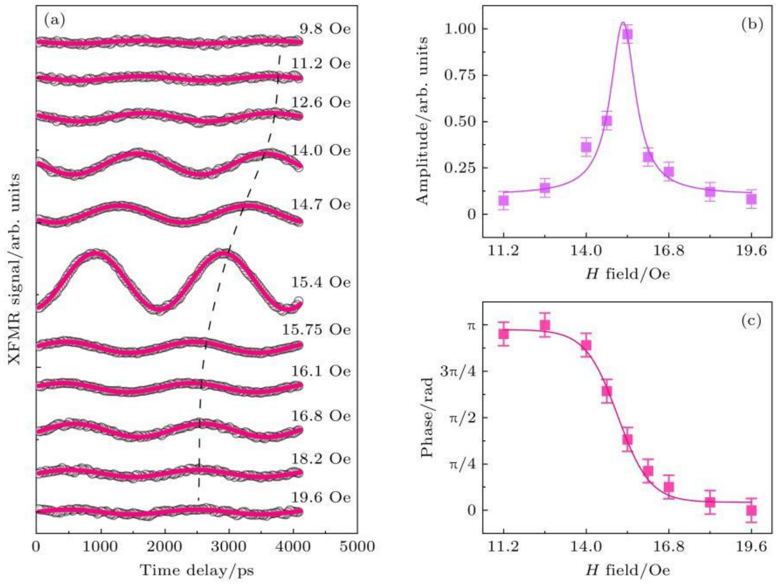

Fig. 8 Phase delay scan (a) at 0.5 GHz under a fixed bias magnetic field, with extracted amplitude (b) and phase (c).

To further quantify the system's phase time resolution, we performed high-precision fitting and residual analysis at an excitation frequency of 6 GHz (Figure 9) to evaluate the signal-to-noise ratio (SNR) of the raw data. The fitting model employs a sinusoidal function of the following form:

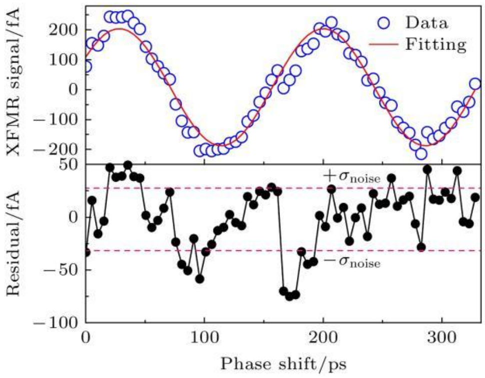

Fig. 9 High-precision fitting and residual analysis at an excitation frequency of 6 GHz.

$$S(\varphi) = A\sin(\varphi + \varphi_0) + B, \quad (4)$$

Here, A represents the signal amplitude (peak intensity), φ denotes the pump-probe phase difference, and φ_0 and B correspond to the initial phase offset and baseline offset, respectively. We calculate the residuals as $r(\varphi) = y(\varphi) - y_{\text{fit}}(\varphi)$. Assuming a Gaussian distribution, we estimate the noise level based on the standard deviation of the residuals, σ_{noise}. In this context, $y(\varphi)$ represents the experimentally measured signal value at phase φ, while $y_{\text{fit}}(\varphi)$ denotes the corresponding function value derived from the aforementioned sinusoidal model fit. The signal-to-noise ratio (SNR) is defined as the ratio of the amplitude to the noise standard deviation: $\text{SNR} = A/\sigma_{\text{noise}}$. This metric characterizes the resolvability of periodic signals against a noise background and intuitively reflects the relative magnitude of the periodic signal compared to the noise intensity. Based on the fit, we obtained an amplitude A of 196 fA and a noise standard deviation σ_{noise} of 30.1 fA (indicated by the red auxiliary line in Figure 9), yielding an SNR of 6.51. We further define the phase time resolution as the minimum phase difference that the system can reliably distinguish or measure. In the presence of noise, a change in phase difference causes a just-detectable change in signal intensity S. Assuming the minimum step size is smaller than the phase time resolution, for small phase changes $\delta\varphi$, the change in signal is approximated as $\Delta S \approx (\mathrm{d}s/\mathrm{d}\varphi)\delta\varphi = A\cos(\varphi + \varphi_0)\delta\varphi$. To accurately resolve the phase value, the condition $\Delta S \geqslant 2.355\sigma$ (resolvability threshold) must be met, implying $\delta\varphi \geqslant 2.355\sigma/|A\cos(\varphi + \varphi_0)|$. Considering the point of fastest amplitude change, where $\cos(\varphi + \varphi_0) = 1$, we derive $\delta\varphi \geqslant 2.355\sigma/A = 2.355/\text{SNR}$. The equivalent phase time resolution is given by $\delta t = (\frac{\delta\varphi}{2\pi})T$, where T is the precession period and $\delta\varphi$ is the phase resolution obtained via sinusoidal fitting. The minimum resolvability is limited by the SNR. Based on the experimental SNR of 6.51, at the point of fastest phase change, the resolution is $\delta t = (\frac{\delta\varphi}{2\pi})T = \frac{2.355}{\text{SNR}\cdot 2\pi}T = 9.37\text{ps}$ (<10 ps). This phase time resolution indicates that the system can reliably distinguish subtle changes on the order of 10 ps or greater during

GHz magnetization precession processes.

4 Discussion

4.1 Summary and Comparison of Global XFMR Light Sources

Currently, synchrotron radiation facilities worldwide with mature XFMR experimental systems remain limited. These systems have developed distinct technical advantages in areas such as time-resolution capabilities, diversity of measurement modes, and SNR optimization. Consequently, they provide crucial experimental support for understanding magnetization dynamics. According to published literature, apart from the BL07U beamline at the SSRF established by our team, five other synchrotron radiation facilities globally have possessed or currently possess XFMR measurement capabilities. These are: the ALS at Lawrence Berkeley National Laboratory (USA), beamline 4.0.2; the Diamond Light Source (DLS) (UK), beamline I10; the Pohang Light Source (PLS) (South Korea), beamline 2A-MS; the ESRF (France), beamline ID08; and the APS at Argonne National Laboratory (USA), beamline 4-ID-C. Among these, the APS in the USA and the ESRF in France were the earliest to conduct XFMR experimental research, dating back to 2004. However, few new XFMR studies from these facilities have been reported in recent years. This decline may be attributed to factors such as larger X-ray pulse widths, limited measurable frequency ranges, overly broad energy coverage, beamline functional restructuring, or the high operational complexity of the technique. Currently, the most active systems are primarily located at the ALS in the USA and the DLS in the UK. The time resolution of the ALS XFMR system is limited by the storage ring pulse width (approximately 70 ps). Nevertheless, its stable signal modulation scheme and high reproducibility have made it a foundational platform for XFMR technology development. The DLS I10 beamline combines XFMR technology with elastic scattering and polarization analysis, extending its application to the study of dynamic evolution in magnetic ordered structures. Although the XFMR setup at the PLS beamline in South Korea is not yet fully open to users, it offers a broader selection range for low photon energies, down to 120 eV. This provides potential advantages for element-specific studies in the low-energy region compared to the aforementioned facilities. Table 1 summarizes the global synchrotron radiation sources that have possessed or currently possess XFMR measurement capabilities, along with their main parameters.

Table 1 Summary of the world's synchrotron radiation sources that have had or currently have XFMR measurement capabilities.

Beamline	APS BL 4-ID-C	ESRF Former BL ID08, Current BL ID32	ALS 4.0.2	DLS I10	PLS 2A-MS	SSRF BL07U
Pulse width/ps	70[32]	100[33]	70[14]	41[23]	100[34]	28.3[27]
Theoretical maximum frequency/GHz	7[32]	5[33]	7[14]	11[23]	5[34]	17[27]
Highest frequency reported in literature/GHz	4.5[32]	2.47[16]	5[14]	6[23]	2.3[35]	6
Spot size/μm^2	100×300[36]	100×10[37]	100×100[38]	200×20[39]	200×1000[40]	120×50[41]
Photon flux/(photons·s-1)	10^{12}@1000 eV[36]	2×10^{13}@700 eV[16]	1×10^{12}@800 eV[38]	1×10^{12}[39]	10^{10}-10^{12}@867 eV[40]	1×10^{12}@867 eV[41]
Energy range/eV	400 -2800[42]	300-1600[37]	400 -1500[38]	400 -2000[39]	100 -1500[40]	50-2000[41]

It is worth noting that Yang et al.[27] successfully established the first domestic XFMR experimental platform featuring picosecond-level time resolution at the BL08U beamline of the SSRF in 2021. However, limited by the experimental conditions at that time, the signal-to-noise ratio (SNR) of the precession curves derived from the experimental data was relatively low, with a time resolution of only 20 ps. Furthermore, the system suffered from issues such as complex sample preparation, low excitation frequencies, limited magnetic fields, and temperature constraints restricted to room temperature. Nevertheless, the construction of this platform provided significant technical references and preliminary experience for the development of our current XFMR system.

4.2 Applications and Technical Upgrades of X-ray Ferromagnetic Resonance

This study developed a high-sensitivity XFMR technique based on synchrotron radiation, achieving phase time resolution at the sub-10 ps level and enabling magnetization dynamics measurements at frequencies up to 6 GHz. Leveraging the excellent narrow temporal pulse width and broad energy coverage of the SSRF, we can further conduct element-, valence-, and lattice-site-resolved studies of ultrafast magnetic precession. This approach reveals the coupling dynamics between different sublattices in ferrimagnetic materials[43,44], which is crucial for understanding multi-sublattice cooperative behaviors in strongly correlated systems[45]. Regarding antiferromagnetic GHz resonance research, we can further develop AC-XMLD (alternating current X-ray magnetic linear dichroism) measurement techniques through temperature control and magnetic field tuning relative to the Néel vector orientation. This allows for the analysis of intrinsic spin dynamics in weak ferromagnetic, compensated ferrimagnetic, and antiferromagnetic systems[25,46]. Simultaneously, focusing on the injection and transport of "orbital currents," we distinguish the respective contributions of spin and orbital polarization based on the orbital Hall effect and orbital torque. By employing thickness modulation and interface engineering design, we systematically investigate the characteristic transport of orbital angular momentum[47,48]. In terms of sample and detection geometry, we adopt different detection modes (fluorescence yield [FY] / luminescence yield [LY]). This extends the measurement scope to thick films and bulk samples with strong spontaneous fluorescence without relying on transmission, thereby obtaining dynamic magnetic signals with high SNR and phase time resolution[49].

Future developments in XFMR technology will advance toward higher phase time resolution, smaller spatial scales, and stronger multi-system synergy. By utilizing the low-alpha mode of the storage ring, it is expected to improve the effective time resolution to <5 ps, further enabling ferromagnetic resonance measurements in the sub-terahertz (sub-THz) frequency range[50]. Combining soft X-ray transmission microscopy (STXM) with nanofocusing techniques allows for the development of a combined "spectroscopy + imaging" measurement mode. This is expected to achieve local magnetic resonance measurements with a spatial resolution of <100 nm[51]. Furthermore, introducing external field couplings such as electric fields, strain, and heat flow will provide novel experimental pathways for studying magnetodynamic processes and their control mechanisms under multi-physics field driving[13]. Meanwhile, with the development of high-harmonic generation (HHG-EUV), it is expected to form a multi-scale research platform integrating "tabletop ultrafast qualitative characterization" and "synchrotron radiation quantitative characterization"[11]. Additionally, we are currently constructing an XFMR experimental system at the high-sensitivity spin spatiotemporal resolution beamline of the Hefei Advanced Light Source (HALS). As a fourth-generation diffraction-limited storage ring light source, HALS offers extremely high brightness and improved SNR, which will significantly shorten measurement times and enable the detection of more complex spin dynamic processes. Moreover, its extremely small spot size (3 μm×3 μm) provides significant advantages for XFMR experiments, laying the foundation for spatially resolved measurements of spin dynamics and spin current transport.

5 Conclusion

Based on the BL07U vector magnet experimental station at the Shanghai Synchrotron Radiation Facility, this study developed and optimized a synchrotron radiation XFMR experimental platform with picosecond-level time resolution precision. We realized the first domestic phase time-resolved XFMR measurement system characterized by high stability, broad bandwidth, and high SNR. The platform employs storage ring master clock locking and lock-in amplification modulation detection techniques, suppressing system noise to the 30 fA level and effectively enhancing the detection sensitivity for weak dynamic magnetic signals. By optimizing the coplanar waveguide structure, stable excitation and response were achieved within the 0.5-6 GHz frequency range. The overall phase time resolution is better than 10 ps, marking that China's synchrotron radiation XFMR technology has reached an internationally advanced level. This technology not only provides an important platform for studying spin and orbital current transport, as well as the dynamics of ferrimagnetic and antiferromagnetic systems, but also lays a solid foundation for future multi-dimensional magnetodynamic measurements at the nanoscale spatial and femtosecond temporal scales.

Data Availability Statement

The associated data for this paper are accessible via the Science Data Bank at https://doi.org/10.57760/sciencedb.j00213.00257.

Some samples for this work were prepared at the Micro and Nano Research and Fabrication Center of the University of Science and Technology of China. Partial data collection benefited from the support of the XMCD-A and XMCD-B beamlines (Suzhou Energy Material Beamline) at the National Synchrotron Radiation Laboratory. We thank the staff of the BL07U beamline at the SSRF for their assistance with XMCD/XAS data collection and system construction.

References

[1] Kirilyuk A, Kimel A V, Rasing T 2010 *Rev. Mod. Phys.* **82** 2731

[2] Walowski J, Münzenberg M 2016 *J. Appl. Phys.* **120** 140901

[3] Zhang W T, Maldonado P, Jin Z M, Seifert T S, Arabski J, Schmerber G, Beaurepaire E, Bonn M, Kampfrath T, Oppeneer P M, Turchinovich D 2020 *Nat. Commun.* **11** 4247

[4] Koopmans B, Van Kampen M, Kohlhepp J T, De Jonge W J M 2000 *Phys. Rev. Lett.* **85** 844

[5] Acremann Y, Strachan J P, Chembrolu V, Andrews S D, Tyliszczak T, Katine J A, Carey M J, Clemens B M, Siegmann H C, Stöhr J 2006 *Phys. Rev. Lett.* **96** 217202

[6] Kittel C 1948 *Phys. Rev.* **73** 155

[7] Tserkovnyak Y, Brataas A, Bauer G E 2002 *Phys. Rev. B* **66** 224403

[8] Wang H L, Du C H, Pu Y, Adur R, Hammel P C, Yang F Y 2013 *Phys. Rev. B* **88** 100406[R]

[9] Liu L Q, Moriyama T, Ralph D C, Buhrman R A 2011 *Phys. Rev. Lett.* **106** 036601

[10] Hoffmann A 2013 *IEEE Trans. Magn.* **49** 5172

[11] Siegrist F, Gessner J A, Ossiander M, Denker C, Chang Y P, Schröder M C, Guggenmos A, Cui Y, Walowski J, Martens U, Dewhurst J K, Kleineberg U, Münzenberg M, Sharma S, Schultze M 2019 *Nature* **571** 240

[12] Tanksalvala M, Kos A, Wisser J, Diddams S, Nembach H T, Shaw J M 2024 *Phys. Rev. Appl.* **21** 064047

[13] Marcham M K, Shelford L R, Cavill S A, Keatley P S, Yu W, Shafer P, Neudert A, Childress J R, Katine J A, Arenholz E, Telling N D, van der Laan G, Hicken R J 2013 *Phys. Rev. B* **87** 180403[R]

[14] Klewe C, Li Q, Yang M M, N’Diaye A T, Burn D M, Hesjedal T, Figueroa A I, Hwang C, Li J, Hicken R J, Shafer P, Arenholz E, van der Laan G, Qiu Z Q 2020 *Synchrotron Radiat. News* **33** 12

[15] Bailey W E, Cheng L, Keavney D J, Kao C C, Vescovo E, Arena D A 2004 *Phys. Rev. B* **70** 172403

[16] Boero G, Rusponi S, Bencok P, Popovic R S, Brune H, Gambardella P 2005 *Appl. Phys. Lett.* **87** 152503

[17] Goulon J, Rogalev A, Wilhelm F, Jaouen N, Goulon Ginet C, Goujon G, Ben Youssef J, Indenbom M V 2005 *J. Exp. Theor. Phys.* **82** 696

[18] Arena D A, Vescovo E, Kao C C, Guan Y, Bailey W E 2006 *Phys. Rev. B* **74** 064409

[19] Baker A A, Figueroa A I, Collins McIntyre L J, van der Laan G, Hesjedal T 2015 *Sci. Rep.* **5** 7907

[20] Baker A A, Figueroa A I, Love C J, Cavill S A, Hesjedal T, van der Laan G 2016 *Phys. Rev. Lett.* **116** 047201

[21] Dąbrowski M, Nakano T, Burn D M, Frisk A, Newman D G, Klewe C, Li Q, Yang M M, Shafer P, Arenholz E, Hesjedal T, van der Laan G, Qiu Z Q, Hicken R J 2020 *Phys. Rev. Lett.* **124** 217201

[22] Burn D M, Zhang S L, Yu G Q, Guang Y, Chen H J, Qiu X P, van der Laan G,

Hesjedal T 2020 *Phys. Rev. Lett.* **125** 137201
[23] Burn D M, Zhang S L, Zhai K, Chai Y S, Sun Y, van der Laan G, Hesjedal T 2020 *Nano Lett.* **20** 345
[24] Li J, Shelford L R, Shafer P, Tan A, Deng J X, Keatley P S, Hwang C, Arenholz E, van der Laan G, Hicken R J, Qiu Z Q 2016 *Phys. Rev. Lett.* **117** 076602
[25] Li Q, Yang M M, Klewe C, Shafer P, N'Diaye A T, Hou D, Wang T Y, Gao N, Saitoh E, Hwang C, Hicken R J, Li J, Arenholz E, Qiu Z Q 2019 *Nat. Commun.* **10** 5265
[26] Kim C, Choi W C, Moon K W, Kim H J, An K, Park B G, Kim H Y, Hong J i, Kim J, Qiu Z Q, Kim Y, Hwang C 2023 *J. Appl. Phys.* **133** 173906
[27] Yang X, Cao J F, Li J Q, Zhu F Y, Yu R, He J, Zhao Z L, Wang Y, Tai R Z 2022 *Nucl. Sci. Tech.* **33** 63
[28] Tai R Z, Zhao Z T 2024 *Nucl. Sci. Tech.* **35** 137
[29] Zhu F Y, Cao J F, Meng X Y, Li J Q, Yu R, Wang Y M, Qiao S, Zhao B, Zhang M Z, Liu Z K, Wang M X, Wang Y, Tai R Z 2024 *Nucl. Sci. Tech.* **35** 130
[30] van der Laan G 2017 *J. Electron Spectrosc. Relat. Phenom.* **220** 137
[31] Gilbert T L 2004 *IEEE Trans. Magn.* **40** 3443
[32] Arena D A, Ding Y, Vescovo E, Zohar S, Guan Y, Bailey W E 2009 *Rev. Sci. Instrum.* **80** 083903
[33] Sévelin Radiguet N, Torchio R, Berruyer G, Gonzalez H, Pasternak S, Perrin F, Occelli F, Pépin C, Sollier A, Kraus D, Schuster A, Voigt K, Zhang M, Amouretti A, Boury A, Fiquet G, Guyot F O, Harmand M, Borri M, Groves J, Helsby W, Branly S P, Norby J, Pascarelli S, Mathon O 2022 *J. Synchrot. Radiat.* **29** 167
[34] Jo W, Lee S, Eom I, Landahl E C 2014 *Rev. Sci. Instrum.* **85** 125112
[35] Kim C, An K, Moon K W, Kim Y, Hwang C 2025 *Curr. Appl. Phys.* **81** 1
[36] Freeland J W, Lang J C, Srajer G, Winarski R, Shu D, Mills D M 2002 *Rev. Sci. Instrum.* **73** 1408
[37] European Synchrotron Radiation Facility https://www.esrf.fr/ID32 [2025-11-01]
[38] The Advanced Light Source https://als.lbl.gov/beamlines/4-0-2/ [2025-10-28]
[39] Diamond Light Source https://www.diamond.ac.uk/Instruments/Magnetic-Materials/I10 [2025-10-25]
[40] Pohang Accelerator Laboratory https://paleng.postech.ac.kr/en/pls/plsbeamLineMap/beam2A/selectView.do [2025-11-20]
[41] Shanghai Advanced Research Institute https://ssrf.sari.ac.cn/dkxzz/tbfs/gsxz_gb/xzdl_tbfs/bl07u/xzjs/ [2025-11-10]
[42] The Advanced Photon Source https://www.aps.anl.gov/Sector-4/4-ID-C

[2025-12-13]

[43] Boero G, Rusponi S, Bencok P, Meckenstock R, Thiele J U, Nolting F, Gambardella P 2009 *Phys. Rev. B* **79** 224425

[44] Warnicke P, Stavitski E, Lee J S, Yang A, Chen Z, Zuo X, Zohar S, Bailey W E, Harris V G, Arena D A 2015 *Phys. Rev. B* **92** 104402

[45] Li T Q, Patz A, Mouchliadis L, Yan J Q, Lograsso T A, Perakis I E, Wang J G 2013 *Nature* **496** 69

[46] Klewe C, Emori S, Li Q, Yang M M, Gray B A, Jeon H M, Howe B M, Suzuki Y, Qiu Z Q, Shafer P, Arenholz E 2022 *New J. Phys.* **24** 013030

[47] Hayashi H, Jo D, Go D, Gao T H, Haku S, Mokrousov Y, Lee H W, Ando K 2023 *Commun. Phys.* **6** 32

[48] Ishii Y, Yamasaki Y, Kozuka Y, Lustikova J, Nii Y, Onose Y, Yokoyama Y, Mizumaki M, Adachi J I, Nakao H, Arima T h, Wakabayashi Y 2024 *Sci. Rep.* **14** 15504

[49] Tröger L, Arvanitis D, Baberschke K, Michaelis H, Grimm U, Zschech E 1992 *Phys. Rev. B* **46** 3283

[50] Huang X B, Safranek J, Corbett J, Nosochkov Y, Sebek J, Terebilo A 2007 *IEEE Particle Accelerator Conference* Albuquerque, NM, USA, June 25–29, 2007 p1308

[51] Bonetti S, Kukreja R, Chen Z, Spoddig D, Ollefs K, Schöppner C, Meckenstock R, Ney A, Pinto J, Houanche R, Frisch J, Stöhr J, Dürr H A, Ohldag H 2015 *Rev. Sci. Instrum.* **86** 093703